Analytical Solutions of Poisson's Equation for Realistic Geometrical Shapes of Membrane Ion Channels

Serdar Kuyucak,[#] Matthew Hoyles,[*#] and Shin-Ho Chung[*]
[*]Protein Dynamics Unit, Department of Chemistry, and [#]Department of Theoretical Physics, Research School of Physical Sciences, Australian National University, Canberra, A.C.T. 0200, Australia

ABSTRACT Analytical solutions of Poisson's equations satisfying the Dirichlet boundary conditions for a toroidal dielectric boundary are presented. The electric potential computed anywhere in the toroidal conduit by the analytical method agrees with the value derived from an iterative numerical method. We show that three different channel geometries, namely, bicone, catenary, and toroid, give similar potential profiles as an ion traverses along their central axis. We then examine the effects of dipoles in the toroidal channel wall on the potential profile of ions passing through the channel. The presence of dipoles eliminates the barrier for one polarity of ion, while raising the barrier for ions of the opposite polarity. We also examine how a uniform electric field from an external source is affected by the protein boundary and a mobile charge. The channel distorts the field, reducing it in the vestibules, and enhancing it in the constricted segment. The presence of an ion in one vestibule effectively excludes ions of the same polarity from that vestibule, but has little effect in the other vestibule. Finally, we discuss how the solutions we provide here may be utilized to simulate a system containing a channel and many interacting ions.

INTRODUCTION

The study of the transport process in membrane ion channels is complicated by the presence of the protein walls, whose interaction with ions and water molecules is not well understood. Ions in solution execute a random Brownian motion and, when an electric field is applied, they acquire a drift velocity. Thus it is this interaction between ions and the electric field (or electric potential profile) in the channel that determines many of the salient properties of ion channels. Finding the electric potential profile everywhere in the channel tends to be difficult. This is because such a profile results from the superposition of electric fields arising from several different sources, and these fields become distorted in a complicated fashion by the low dielectric wall represented by the protein-water interface. Among the sources that contribute to the electric field in the channel are 1) the membrane potential, 2) charge residues on the protein wall, 3) ions inside or in the vicinity of the channel, and 4) charges induced on the protein wall by those ions. The last two sources interact dynamically: as an ion moves from one position to another, the pattern of induced charges changes, and the induced surface charges together impede the motion of the ion as it moves toward the narrow neck region of the channel.

In the past, studies of energy barriers and electric field profiles in the transmembrane ionic conduit have been carried out almost exclusively in cylindrical geometry (Jordan, 1981, 1982, 1983; Levitt, 1978a,b). One of the advantages of the cylindrical geometry is the availability of simple analytical solutions to Poisson's equation. In a cylindrical geometry, however, the transport problem is reduced to one dimension, and its application as a realistic model of channels beyond the gramicidin channel remains doubtful. A recent numerical study of the ion-channel potential for different channel geometries has demonstrated that vestibules, in the form of a biconical or catenary shape, have dramatically different potential profiles compared to cylindrical pores (Hoyles et al., 1996). Thus it appears that for realistic studies of ion transport in biological channels, one must employ geometries that more accurately describe the channel.

Electric potential profiles in ion channels of any arbitrary geometry can be generated numerically by solving Poisson's equation iteratively. In such a numerical method (e.g., Hoyles et al., 1996), the boundary is divided into a large number of small sectors, and the charge density appearing on each sector due to the electric field from an ion in the electrolyte solution as well as that emanating from all other boundary sectors is calculated. The computational effort required is modest for constructing the profile of the energy barrier as a single ion moves toward the narrow neck region from the mouth of the vestibule. However, it becomes impractical to attempt to simulate, using such a numerical method, the motion of many ions in the vicinity of the channel. To study the dynamics of ions in a channel, one needs to compute the forces acting on each of the ions due to various sources, including induced and fixed charges on the wall and the applied electrical field, and couple these results with Brownian dynamics simulations. Because this computation has to be repeated at every step, the existence of analytical solutions in a relevant geometry is imperative for simulations at realistic time scales. Analytical solutions of Poisson's equation would also be helpful in other methods utilizing the Nernst-Planck or Boltzmann equations.

Received for publication 15 April 1997 and in final form 21 October 1997.
Address reprint requests to Dr. Shin-Ho Chung, Department of Chemistry, Australian National University, Canberra, A.C.T. 0200, Australia. Tel.: 61-2-6249-2024; Fax: 61-2-6247-2792; E-mail: shin-ho.chung@anu.edu.au.

0006-3495/98/01/22/15 $2.00

We present here solutions of Poisson's equation for a toroidal channel. Of all of the coordinate systems in which Poisson's equation separates, the toroidal coordinates come closest to forming a realistic channel boundary. First we show that the analytical solutions for the electric potential are in good agreement with those obtained from the numerical method. Next we study the sensitivity of the potential profile to the channel shape by comparing the energy barriers presented to an ion traversing the central axis of biconical, catenary, and toroidal channels. These results confirm that the toroidal channel, for which analytical solution of Poisson's equation exists, is a good approximation of biological ion channels. Using the analytical solutions, we demonstrate that the orientation of dipoles near the constricted region of the channel renders it permeable to cations, while making it virtually impermeable to anions. We also show that the electric field in the channel, far from being constant, is enormously enhanced in the transmembrane segment by the dielectric boundary. We reveal how the pattern of the electric potential profile seen by other ions changes dynamically as a cation moves from one side of the channel to the other. Finally, we discuss how the solutions we provide here may be extended to cope with transport processes occurring in dynamical situations and suggest further studies that our results now make possible.

IDEALIZED MODEL CHANNEL

We wish to obtain analytical solutions of Poisson's equation for a realistic channel geometry and then study the behavior of charged particles in or in the vicinity of this idealized ion channel. In this and the companion paper (Li et al., 1997), we compute the force experienced by an ion as it traverses the toroidal channel under various conditions and deduce its molecular trajectories by using stochastic dynamics simulations. The ultimate objective of theoretical studies such as ours is to relate the macroscopically observable properties of ion channels, such as conductance, current-voltage relationships, conductance-concentration curves, and gating behavior, to the details of the intermolecular potential operating between water molecules, ions, and protein wall containing dipoles and charge residues.

To gain insight into the permeation of ions across the channel, it is desirable to simulate the motion of all water molecules and ions in a channel and surroundings (~10,000 molecules) for a period long enough to measure conductance. This is not technically feasible at present. We therefore make the following simplifications and idealizations about our model channel to make computations tractable.

Shape of the channel

We form the channel surface by rotating by 360° along the z axis a closed circle, the radius of which is 40 Å and the center of which is located at $x = 44$ Å. The narrowest segment of the toroidal channel has a radius of 4 Å, and two vestibules extend to 40 Å from the midline. The radius we selected for the constricted segment corresponds that of the potassium ion with its first hydration shell. The shape of the ACh channel determined by Toyoshima and Unwin (1988) is better approximated by an hourglass than a toroid, but the analytical solutions for Poisson's equation for such a dielectric boundary cannot be derived. It will be shown later that three different shapes of the vestibule (bicone, catenary, and toroid) give broadly similar potential profiles (see Fig. 3).

Our model is only of the channel, and does not explicitly include the surrounding lipid membrane. The analytical solution is strictly for a toroidal dielectric boundary, and cannot be extended to include an infinite slab as well, as would be needed to represent the membrane. The model does have, however, a large outside radius (44 Å) compared to that of the ACh channel (~25 Å), and the exterior surface of the channel could be considered to include part of the surrounding membrane. We have ascertained that the omission of the membrane makes virtually no difference to the potential in the pore. It is the inside boundary of the channel, between the water in the pore and the protein wall, that contributes the majority of the potential. To demonstrate the limited effect of the outside boundary, we reduced the outside radius of a catenary channel (similar to the one in Fig. 3 *A*) from 43 Å to 28 Å, while keeping all other dimensions constant. The potential barrier height was reduced by only 2%. Similarly, when we increased the catenary channel's outside radius from 43 Å to 73 Å, the barrier height increased by less than 1%.

Water as a continuum

We treat the water as a continuum and the ions as individual entities. Individual ions are assumed to move under the influence of electrostatic forces emanating from other ions, fixed charges, the applied electric field, and the dielectric boundary. In the following paper (Li et al., 1997), where Brownian dynamics simulations are carried out, the effects of solvation and the structure of water are taken into account by frictional and random forces. In applying the theory of macroscopic electrostatics to describe long-range interactions between particles, we use the dielectric constant from bulk. Confined in each channel vestibule are ~500 water molecules. The effective dielectric constant of such "vicinal" water (Drost-Hansen and Singleton, 1992) is not known; this question deserves further theoretical and experimental attention. Almost certainly the effective dielectric constant will be lower than that in bulk water. We investigate how the estimated potential barrier will be affected when the effective dielectric constant in the vestibule is assumed to be 20 and 40, instead of being 80 (see Fig. 8). Conclusions drawn and inferences made from electrostatics are not valid, however, in regions that are small compared to the diameter of water and ion molecules. In the constricted region of the channel, where the radius is less than 4–5 Å, water molecules are ordered and are not free to align with

the external field. The representation of the dielectric as a continuous medium in such a region is a very poor approximation. To elucidate the permeation process inside this region, molecular dynamics calculations such as those reported for the gramicidin channel (e.g., Roux and Karplus, 1991) will be needed.

Smooth water-protein interface

We model the water-protein interface as a single, sharp and rigid boundary between dielectrics. In reality, however, the channel wall is not made of a structureless dielectric material. Instead, its surface is likely to be lined with hydrophilic and polar side chains, although their type, orientation, and density remain to be determined. Owing to the presence of these polar groups on the protein wall, there will be a gradual change in the orientation of the water molecules; those water molecules located nearer to the water-protein interface tend to be more ordered than those further away from it. The polar groups and the ordered water near the interface are not explicitly included in our model, being represented by the dielectric boundary. It is possible to treat the interface more accurately by assuming that there is a thin boundary layer with a dielectric constant intermediate between those of protein and water. We have shown elsewhere that the magnitude of error introduced by ignoring the intermediate dielectric layer is negligible (Hoyles et al., 1996). Moreover, we show in the following paper (Li et al., 1997) that ions in the vestibules tend to be near the central axis, away from the channel wall.

Dipole rings at the transmembrane segment

We investigate how the permeation of ions across the channel is influenced by the presence and absence of dipoles on the protein wall. The number, magnitude, and location of dipoles or charge moieties on the protein wall of biological ion channels are unknown. For simplicity, we assume that these charge moieties are located near the constricted region of the channel, as suggested by structural studies (e.g., Unwin, 1989), and represent them as a ring of four dipoles at each side of the membrane segment, oriented perpendicular to the central channel axis. These fixed charges represent the charged side chains thought to form a ring around the entrance of the constricted region, and their nearby countercharges. For convenience we adjust the amount of charge rather than the number or positions of the charges, but in reality the side chains would have one electron charge each. Polar groups located in the constricted segment of the channel that may rotate in and out to form temporary hydrogen bonds with an ion navigating across it, as found in gramicidin A pores, are not explicitly modeled in this study. This will be the subject of a future investigation using molecular dynamics calculations.

The applied electric field

There are two ways of providing the driving force that can move the ion across the channel: a potential difference or a concentration gradient between the two faces of the channel. On a macroscopic level these two are equivalent, being coupled by the Nernst-Planck equation, and concentration differences are often expressed as an equivalent potential. On a microscopic level, however, the physical processes are very different. An electric potential gradient applies a force to every ion, causing it to acquire an average drift velocity. A concentration gradient causes no forces on the ions and no average drift velocity, but their random Brownian motion carries the ions down the concentration gradient. To mimic the real situation, the potential gradient should be generated by a diffuse cloud of unpaired positive ions, representing a surface charge density, in one reservoir and a cloud of unpaired negative ions in the other. The number of unpaired ions must be, to be consistent with the situation in real biological membranes, a small fraction of the total number of the ionic species present. Thus the clouds of surface charges cannot be represented explicitly within the simulation unless the size of the simulation is expanded by a factor of 100. It is impractical to generate a potential difference with clouds of the ionic atmosphere, although this method is self-consistent and theoretically correct.

We therefore provide the driving force by applying an external electric field, which represents the average effect of the ionic clouds. From a number of current-voltage relationships obtained with a different number of ions in two reservoirs, we have ascertained that the reversal potential occurs at a potential close to that predicted by the Nernst equation. In our simulation system, as in a macroscopic system composed of an ensemble of real biological channels, the force driving ions across the membrane can be provided either by an externally applied electric field or by a concentration gradient.

SOLUTIONS OF BOUNDARY-VALUE PROBLEMS

Toroidal coordinates

The system of toroidal coordinates (μ,η,ϕ) is illustrated in Fig. 1. The coordinate μ is defined as $\log(PL'/PL)$, where L and L' are the limiting points of a set of coaxial circles. The constant $\mu = \mu_1$ defines the surface of a torus. When circles of progressively increasing radii are drawn (*dotted lines* in Fig. 1), their centers move out on the x axis toward infinity. Thus, as μ decreases progressively from ∞ to 0, the circles grow from the point at L (zero radius) to the z axis (infinite radius with center at infinity). The coordinate η is defined by the angle LPL' and has the range $[0, 2\pi]$. For a given μ, η traces a circle of a fixed radius as it changes from 0 to 2π, as indicated in Fig. 1. Finally, ϕ is the usual azimuthal angle about the symmetry axis z with the range $[0, 2\pi]$. As a circle is revolved around the z axis by 360° counterclockwise, a toroidal shape is generated. A point anywhere inside and

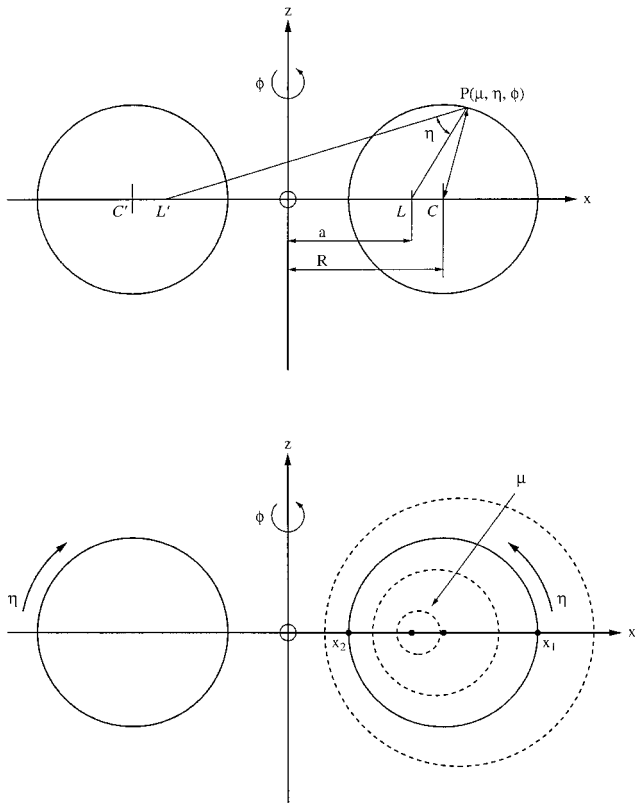

FIGURE 1 Toroidal coordinate system. A torus is generated by rotating the two circles shown in the upper panel by 180° along the z axis. A point P anywhere in space can be defined by (μ, η, ϕ). The coordinate μ describes a ring of circles. The radius of the circle decreases progressively, and its center moves in from ∞ to point L on the x axis as μ increases from 0 to ∞. For a given μ, η traces a circle of fixed radius as it goes from 0 to 2π, with $\eta = 0$ furthest from the z axis, and $\eta = \pi$ nearest. The coordinate ϕ is the azimuthal angle about the z axis.

outside of the torus, as well as on its surface, can be represented by μ, η, and ϕ.

The toroidal coordinates are related to the Cartesian ones through the following set of equations (Morse and Feshbach, 1953):

$$x = \frac{a \sinh \mu \cos \phi}{\cosh \mu - \cos \eta}, \quad y = \frac{a \sinh \mu \sin \phi}{\cosh \mu - \cos \eta}, \quad z = \frac{a \sin \eta}{\cosh \mu - \cos \eta} \tag{1}$$

In the x-z plane, the circle describing the toroidal surface will intersect the positive x axis twice, x_1 at $\eta = 0$ and x_2 at $\eta = \pi$. Thus the radius r of the torus is related to the toroidal coordinates by the expression

$$x_1 - x_2 = \frac{a \sinh \mu_1}{\cosh \mu_1 - 1} - \frac{a \sinh \mu_1}{\cosh \mu_1 + 1} = \frac{2a \sinh \mu_1}{\cosh^2 \mu_1 - 1} = \frac{2a}{\sinh \mu_1} = 2r \tag{2}$$

Similarly, the distance from the origin to the center of the torus R can be expressed in terms of the toroidal coordinates as

$$R = x_2 + \frac{x_1 - x_2}{2} = a\left(\frac{\sinh \mu_1}{\cosh \mu_1 + 1} + \frac{1}{\sinh \mu_1}\right) = a \frac{\cosh \mu_1}{\sinh \mu_1} = a \coth \mu_1 \tag{3}$$

Thus, as η changes from 0 to 2π, constant μ_1 follows a circle of the minor radius, $r = a/\sinh \mu_1$, centered at the major radius $R = a \coth \mu_1$. By rotating the two circles around the perpendicular z axis, the full toroidal boundary is generated.

We note that the ratio between the minor and major radii, $r/R = 1/\cosh \mu_1$, is independent of a and determines the diameter of the constricted region of the model channel. For $\mu = 0$, both r and R are infinite, and the circle becomes the z axis. In the opposite limit, $\mu = \infty$, the major and minor radii coincide, i.e., $R = a$ and $r = 0$, and the toroid becomes a ring of radius a around the z axis.

Solutions of Laplace's and Poisson's equations

Solution of Laplace's equation in toroidal coordinates is given in terms of the trigonometric functions for η and ϕ, and the toroidal harmonics (Legendre functions of half-order) $P^{m}_{n-1/2}(\cosh \mu)$, $Q^{m}_{n-1/2}(\cosh \mu)$. The most general solution can be written as

$$\varphi = f(\mu, \eta) \sum_{n=0}^{\infty} \sum_{m=0}^{\infty} [A_{nm} Q^{m}_{n-1/2}(\cosh \mu) + B_{nm} P^{m}_{n-1/2}(\cosh \mu)] \times \cos n(\eta - \eta_{nm}) \cos m(\phi - \phi_{nm}) \tag{4}$$

where

$$f(\mu, \eta) = \sqrt{\cosh \mu - \cos \eta} \tag{5}$$

and the coefficients A_{nm}, B_{nm}, η_{nm}, ϕ_{nm} are to be determined from boundary conditions.

The potential due to a point charge q at $\mathbf{r}_0 = (\mu_0, \eta_0, \phi_0)$ is given by (Morse and Feshbach, 1953)

$$\frac{q}{|\mathbf{r} - \mathbf{r}_0|} = \frac{q}{\pi a} f(\mu, \eta) f(\mu_0, \eta_0) \sum_{n=0}^{\infty} \sum_{m=0}^{\infty} (2 - \delta_{n0})(2 - \delta_{m0}) \frac{\Gamma(n - m + 1/2)}{\Gamma(n + m + 1/2)} \times \cos n(\eta - \eta_0) \cos m(\phi - \phi_0) \cdot \begin{cases} P^{m}_{n-1/2}(\cosh \mu) Q^{m}_{n-1/2}(\cosh \mu_0) & \mu < \mu_0 \\ Q^{m}_{n-1/2}(\cosh \mu) P^{m}_{n-1/2}(\cosh \mu_0) & \mu > \mu_0 \end{cases} \tag{6}$$

The change in the μ solutions reflects the fact that $P^{m}_{n-1/2}$ diverges as $\mu \to \infty$ and $Q^{m}_{n-1/2}$ diverges as $\mu \to 0$. Solution

of Poisson's equation for the system of a point charge outside the toroidal boundary $\mu = \mu_1 > \mu_0$, with dielectric constants ϵ_{One} outside and ϵ_{Two} inside the torus, can be found by superposing the potentials in Eqs. 4 and 6. As usual in such boundary value problems, the ϕ solutions are decoupled, and the phases ϕ_{nm} in Eq. 4 must be coherent with ϕ_0, so that $\phi_{\mathrm{nm}} = \phi_0$ for all n, m. The same argument, however, does not hold for the η solutions. Because of the square root factors f (Eq. 5), there is coupling between different coefficients, and the phase factors η_{nm} are not necessarily coherent with η_0. This is a distinctive feature of the toroidal coordinates, and complicates solutions of electrostatic problems in comparison with other coordinate systems. With these caveats, the superposed potential can be written as

$$\varphi_{\mathrm{in}} = f(\mu, \eta) \sum_{\mathrm{n}=-\infty}^{\infty} \sum_{\mathrm{m}=0}^{\infty} A_{\mathrm{nm}} Q^{\mathrm{m}}_{\mathrm{n}-1/2}(\cosh \mu) \cdot \exp[in(\eta - \eta'_{\mathrm{nm}})] \cos m(\phi - \phi_0)$$

$$\varphi_{\mathrm{out}} = f(\mu, \eta) \sum_{\mathrm{n}=-\infty}^{\infty} \sum_{\mathrm{m}=0}^{\infty} [B_{\mathrm{nm}} P^{\mathrm{m}}_{\mathrm{n}-1/2}(\cosh \mu) \exp[in(\eta - \eta''_{\mathrm{nm}})] + C_{\mathrm{nm}} Q^{\mathrm{m}}_{\mathrm{n}-1/2}(\cosh \mu) \exp[in(\eta - \eta_0)]] \cdot \cos m(\phi - \phi_0) \quad (7)$$

where

$$C_{\mathrm{nm}} = \frac{1}{4\pi\epsilon_0\epsilon_1} \frac{q}{\pi a} f(\mu_0, \eta_0)(2 - \delta_{\mathrm{m}0}) \frac{\Gamma(n - m + 1/2)}{\Gamma(n + m + 1/2)} \cdot P^{\mathrm{m}}_{\mathrm{n}-1/2}(\cosh \mu_0) \quad (8)$$

are constant coefficients. In Eq. 7, we used the $\mu > \mu_0$ solution for the point charge (Eq. 6), as it is the appropriate one for the boundary at $\mu = \mu_1$. Also, we replaced the cosines with exponentials for the η solutions, because it simplifies the boundary matching.

Applying the usual boundary conditions at $\mu = \mu_1$,

$$\varphi_{\mathrm{in}} = \varphi_{\mathrm{out}}, \quad \epsilon_2 \frac{\partial \varphi_{\mathrm{in}}}{\partial(\cosh \mu)} = \epsilon_1 \frac{\partial \varphi_{\mathrm{out}}}{\partial(\cosh \mu)} \quad (9)$$

we obtain the following equations for every m:

$$\sum_{\mathrm{n}=-\infty}^{\infty} A_{\mathrm{nm}} Q \exp[in(\eta - \eta'_{\mathrm{nm}})] = \sum_{\mathrm{n}=-\infty}^{\infty} [B_{\mathrm{nm}} P \exp[in(\eta - \eta''_{\mathrm{nm}})] + C_{\mathrm{nm}} Q \exp[in(\eta - \eta_0)]] \quad (10)$$

$$\epsilon_2 \sum_{\mathrm{n}=-\infty}^{\infty} A_{\mathrm{nm}} (fQ' + f'Q) \exp[in(\eta - \eta'_{\mathrm{nm}})] = \epsilon_1 \sum_{\mathrm{n}=-\infty}^{\infty} [B_{\mathrm{nm}} (fP' + f'P) \exp[in(\eta - \eta''_{\mathrm{nm}})] + C_{\mathrm{nm}} (fQ' + f'Q) \exp[in(\eta - \eta_0)]] \quad (11)$$

Here we have introduced the compact notation for the constants, $P = P^{\mathrm{m}}_{\mathrm{n}-1/2}(\cosh \mu_1)$, $Q = Q^{\mathrm{m}}_{\mathrm{n}-1/2}(\cosh \mu_1)$ and $f = f(\mu_1, \eta)$. Similarly, the primes over P, Q, and f denote derivatives with respect to cosh μ evaluated at $\mu = \mu_1$. These equations can be further simplified by introducing the complex coefficients

$$A'_{\mathrm{nm}} = A_{\mathrm{nm}} \exp[-in\eta'_{\mathrm{nm}}], \quad B'_{\mathrm{nm}} = B_{\mathrm{nm}} \exp[-in\eta''_{\mathrm{nm}}], \quad C'_{\mathrm{nm}} = C_{\mathrm{nm}} \exp[-in\eta_0] \quad (12)$$

Substituting the above coefficients in Eqs. 10 and 11, we obtain

$$\sum_{\mathrm{n}=-\infty}^{\infty} A'_{\mathrm{nm}} Q \exp[in\eta] = \sum_{\mathrm{n}=-\infty}^{\infty} [B'_{\mathrm{nm}} P + C'_{\mathrm{nm}} Q] \exp[in\eta] \quad (13)$$

$$\epsilon_2 \sum_{\mathrm{n}=-\infty}^{\infty} A'_{\mathrm{nm}} (fQ' + f'Q) \exp[in\eta] = \epsilon_1 \sum_{\mathrm{n}=-\infty}^{\infty} [B'_{\mathrm{nm}} (fP' + f'P) \exp[in\eta] + C'_{\mathrm{nm}} (fQ' + f'Q) \exp[in\eta]] \quad (14)$$

Equation 13 now holds for each n, and hence we can solve for B'_{nm} in terms of A'_{nm}:

$$B'_{\mathrm{nm}} = (A'_{\mathrm{nm}} - C'_{\mathrm{nm}}) Q/P \quad (15)$$

Substituting B'_{nm} in Eq. 14 and collecting similar terms gives

$$\sum_{\mathrm{n}=-\infty}^{\infty} A'_{\mathrm{nm}} [\epsilon_2 (fQ' + f'Q) - \epsilon_1 (fP' + f'P) Q/P] \exp[in\eta] = \epsilon_1 \sum_{\mathrm{n}=-\infty}^{\infty} C'_{\mathrm{nm}} f(Q' - P'Q/P) \exp[in\eta] \quad (16)$$

Using $f' = 1/2f$ and substituting back $f^2 = \cosh \mu_1 - \cos \eta$, Eq. 16 can be put in the form

$$2(\cosh \mu_1 - \cos \eta) \sum_{n=-\infty}^{\infty} A'_{nm}(\epsilon_2 Q' - \epsilon_1 P' Q/P)\exp[in\eta]$$

$$+ (\epsilon_2 - \epsilon_1) \sum_{n=-\infty}^{\infty} A'_{nm}\, Q \exp[in\eta] \qquad (17)$$

$$= 2\epsilon_1(\cosh \mu_1 - \cos \eta) \sum_{n=-\infty}^{\infty} C'_{nm}(Q' - P'Q/P)\exp[in\eta]$$

Notice that the cos η factors in the front leads to coupling of neighboring coefficients, so that Eq. 17 cannot be solved trivially, as typically encountered in boundary value problems involving spherical or cylindrical coordinate systems. Fourier analysis of the series in Eq. 17 in η (i.e., multiplying by either sin $n'\eta$ or cos $n'\eta$ and integrating from $0 - 2\pi$) gives

$$\sum_{n=-\infty}^{\infty} [(2 \cosh \mu_1(\epsilon_2 Q' - \epsilon_1 P' Q/P) + (\epsilon_2 - \epsilon_1)Q)\delta_{n',n}$$

$$- (\epsilon_2 Q' - \epsilon_1 P' Q/P)(\delta_{n',n+1} + \delta_{n',n-1})]A'_{nm}$$

$$= \epsilon_1 \sum_{n=-\infty}^{\infty} C'_{nm}(Q' - P'Q/P)[2 \cosh \mu_1 \delta_{n',n}$$

$$- (\delta_{n',n+1} + \delta_{n',n-1})] \qquad (18)$$

Introducing further,

$$E_n^m = (\epsilon_2 Q' - \epsilon_1 P' Q/P)A'_{nm}$$

$$q_n^m = 2 \cosh \mu_1 + \frac{(\epsilon_2 - \epsilon_1)Q}{\epsilon_2 Q' - \epsilon_1 P' Q/P}$$

$$\lambda_n^m = \epsilon_1(Q' - P'Q/P)C'_{nm} \qquad (19)$$

we obtain the following second-order difference equation for the coefficients E_n^m:

$$E_{n+1}^m - q_n^m E_n^m + E_{n-1}^m = \lambda_{n+1}^m - 2 \cosh \mu_1 \lambda_n^m + \lambda_{n-1}^m \qquad (20)$$

The real and imaginary parts of this equation must be satisfied separately, leading to two difference equations which, through Eqs. 12 and 19, determine both the amplitude A_{nm} and the phase η'_{nm}. Equation 20 also arises in the problem of a dielectric torus in a uniform electric field (Love, 1972), and can be solved using techniques of the Green function. Because it is rather technical, a sketch of the solution is given in the Appendix. As seen from Eq. 31, the solution involves an infinite sum of series of products. Therefore, for a fast, yet accurate computation of the potential, an efficient evaluation of the coefficients E_n is necessary. A properly optimized computer code has been written for this purpose, which computes the electric potential for an arbitrary number of ions under an applied electric field.

Application of external electric field

The solution for a uniform electric field ε_0, applied along the symmetry axis of the torus, follows the same lines as above, but is much simpler (Love, 1972). Because of the axial symmetry, the potential is independent of the coordinate ϕ. Hence the m-sums in Eq. 7 are suppressed. Furthermore, there are no phase differences in the η solutions, i.e., they are given by exp[$in\eta$] everywhere. The potential for a uniform field in toroidal coordinates is given by

$$\varphi_{ap} = \varepsilon_0 z$$

$$= \varepsilon_0 \frac{\sqrt{8}a}{i\pi} f(\mu, \eta) \sum_{n=-\infty}^{\infty} nQ_{n-1/2}(\cosh \mu)\exp[in\eta] \qquad (21)$$

Superposing φ_{ap} with the free fields in Eq. 4, and applying the boundary conditions, one obtains again a second-order difference equation as in Eq. 20, but without the m indices. The coefficients E_n and q_n are the same as in Eq. 19, and λ_n is modified to

$$\lambda_n = \varepsilon_1(Q' - P'Q/P)\varepsilon_0 \frac{\sqrt{8}a}{\pi} n \qquad (22)$$

The solution of this difference equation is described in the Appendix.

Calculation of force and potential energy

The electric potential and field from multiple ions and an applied electric field are built up by using the principle of superposition. Because we assume that the dielectrics are linear, any number of permanent charges, as well as the applied field, can be included simply by adding together their solutions for the same dielectric boundary. The electric field and potential at the position of an ion are therefore the sum of that due to the other ions, the applied field, the surface charges induced by these, and the surface charges induced by that particular ion.

The force on the ion is simply the total field multiplied by the charge on the ion, but there is a subtlety in the calculation of the ion's potential energy. The potential energy due to the other ions, the applied field, and the charges they induce is the electric potential times the ion's charge. However, the potential energy due to the surface charges induced by the ion itself is only half the electric potential times the charge. This can be seen by imagining the charge Q on the ion being built up as infinitesimal charges dq being brought in from infinity. Whereas the electric potential due to the other ions remain the same throughout, that induced by the ion increases from zero to its full value Q as the charge is built up. This involves integrating q dq from 0 to Q—hence

the factor of one-half. Our program takes account of this by calculating the total field and potential at the postion of an ion, as well as the potential due only to the ion's interaction with the boundary. It then substracts half of this self-potential from the total for the purpose of calculating the potential energy.

Fixed charges in the protein wall are included in the same way as ions. The only change is that they require a slightly different analytical solution, because they are inside the toroidal boundary, not outside. The form of Equation 6 with $\mu = \mu_1 < \mu_0$ needs to be used, and corresponding changes need to be made for the rest of the solution.

RESULTS

Validation of analytical solutions

To ensure that the analytical solutions of Poisson's equation give the correct value of the electric potential anywhere in space, we need to compare the analytical results with those obtained from an iterative numerical method. For this purpose, we examine the potential barrier presented to a cation and the magnitude of a repulsive force the ion experiences as it moves along the central axis of the channel. The minor radius r and the major radius R in this and all subsequent simulations are fixed at 40 Å and 44 Å, respectively. Thus the narrowest segment of the channel has the radius of 4 Å, approximately equal to that of a sodium ion with its primary hydration shell. It is assumed that there are no charge residues on the protein wall, and there is no external electrical field across the channel.

In Fig. 2 the values calculated from the analytical solution (*solid lines*) are superimposed on those calculated by using the iterative numerical methods (*filled and open circles*). For the numerical calculations, the toroidal surface is divided into 1600 sectors, the size of the sectors being smallest at the narrow channel region and becoming progressively larger at the wider region of the vestibules. As the ion moves from the mouth of the toroidal channel to its narrowest segment, the height of the energy barrier increases, first slowly and then steeply, to $\sim 15 \times 10^{-21}$ J or 3.7 kT_r, where k is the Boltzmann constant and $T_r = 298$ K (Fig. 2 *A*). Throughout we will refer to the energy in room temperature units; 1 $kT_r = 4.114 \times 10^{-21}$ J = 2.478 kJ/mol. Similarly, the repulsive force presented to the ion resulting from the induced charges on the dielectric boundary increases to ~8 pN at the narrow segment of the channel (Fig. 2 *B*). The values derived from the iterative method differ at most by 1.5% from those obtained from the analytical solution. These small discrepancies stem from the finite sizes of sectors used in the numerical method, and can be reduced by choosing smaller sector areas. We thus conclude that our analytical solutions give the correct values of electric potentials and forces acting on charged particles at all points in space.

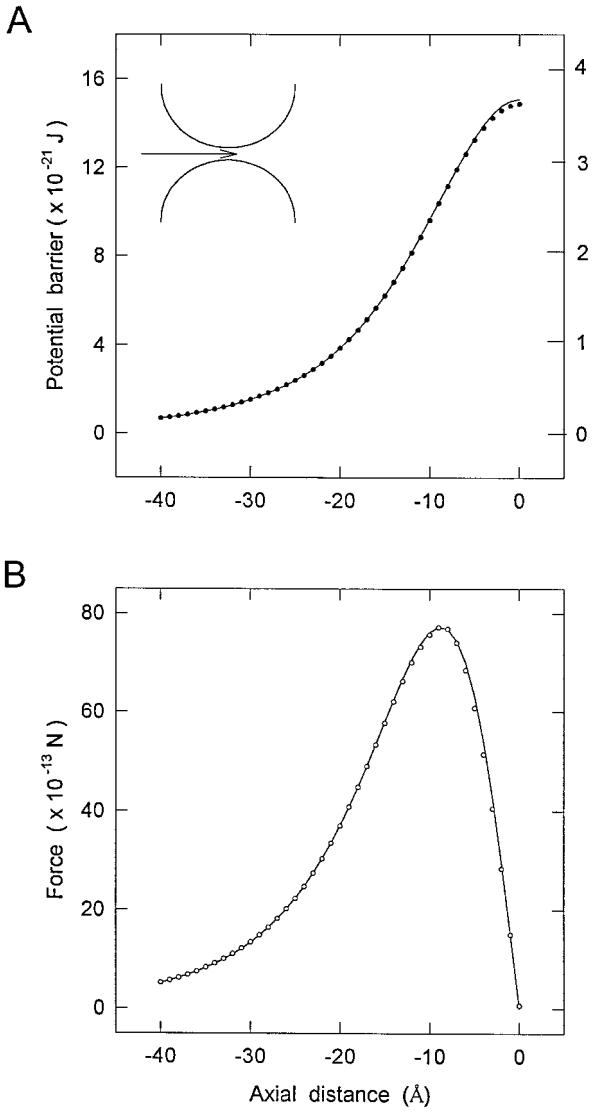

FIGURE 2 Validation of analytical solutions. An ion is moved from the wide end of the vestibule ($z = -40$ Å) to the narrowest segment of the channel ($z = 0$), in steps of 1 Å, and the potential barrier and the force impinging on it at each position are computed both analytically and numerically. The dielectric constants of water and of the channel wall are assumed to be 80 and 2, respectively. (*A*) The potential profile computed numerically (●) is compared with that computed analytically (——). In this and subsequent figures, the height of the potential barrier is also shown in room temperature units, kT_r, where $T_r = 298$ °K and k is the Boltzmann constant (1.38×10^{-23} JK^{-1}). (*B*) The z component of the force impinging on the ion at each position as it moves along the central axis of the pore is computed numerically (○) and plotted against the axial distance. The values derived from the analytical solutions (——) are superimposed on the numerical data.

Insensitivity to the vestibular shape

The profile of the energy barrier an ion needs to surmount is not critically dependent on the shape of the channel vestibule. Fig. 3 *A* shows cross-sectional outlines of biconical, catenary, and toroidal channels. For each of the three shapes of the channels examined, the radius of the narrowest segment is kept constant at 4 Å, and the vestibule is ex-

tended to 40 Å from it. The biconical channel has a cylindrical neck region of length 10 Å, and conical vestibules with a side length of 36 Å and an angle of 18°. The vestibule of the catenary channel, which closely matches the shape of the ACh channel deduced by electron microscope image reconstruction and crystallographic methods (Toyoshima and Unwin, 1988), is generated by a hyperbolic cosine function, $y = a\cosh(x/a)$, where $a = 4.75$ Å. The radius of the entrance of the vestibule is fixed at 15 Å. An ion is placed on the central axes of these model channels, and then the potential energies, as it moves along the central trajectories in 1-Å steps, are tabulated. The potential energy profiles obtained from three different shapes of the channels are shown in Fig. 3 *B*. The values for the biconical (*filled circles*) and catenary channels (*open circles*) are calculated numerically, whereas those for the toroidal channel (*continuous line*) are computed analytically. Except for the initial segment, the potential profiles of three different model channels are broadly similar. The wide radius at the entrance of the vestibule of the toroidal channel, compared to that of the catenary channel, is reflected in the low energy barrier an ion encounters in the first 20 Å as it traverses the channel.

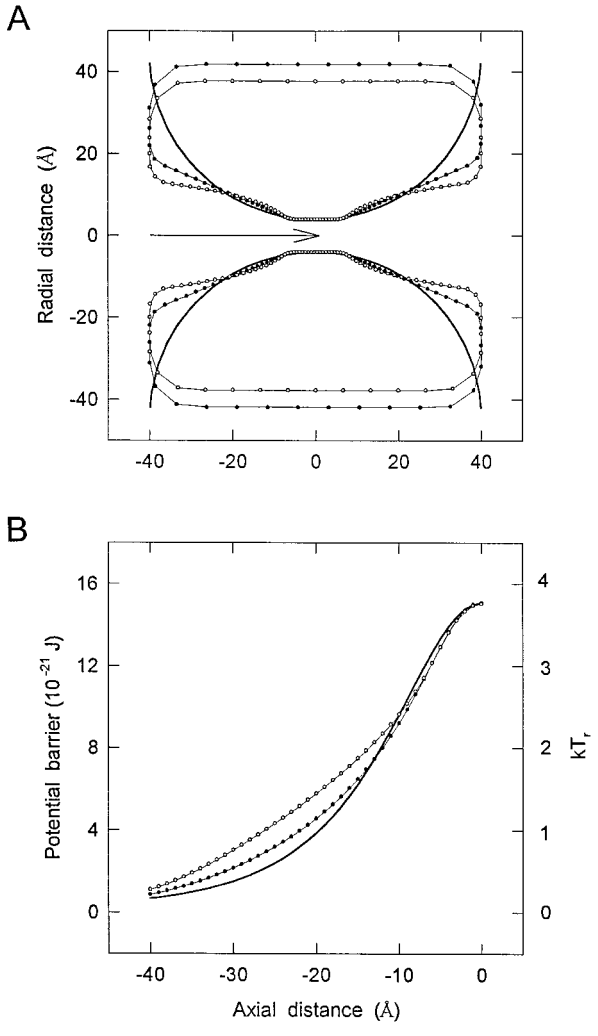

FIGURE 3 Three model channels. (*A*) Three closed curves outlined by solid lines, filled circles, and open circles are rotated along the (horizontal) symmetry axis to generate the surfaces of the toroidal, biconical, and catenary channels, respectively. The radii of the narrowest segments of all three channels are 4 Å. The ion moves along the *z* axis, as indicated by the arrow. (*B*) The potential barriers at each location along the ion's trajectory for the toroidal (——), biconical (●), and catenary (○) channels are shown.

Electric field in the channel

In the presence of the membrane potential, the electric field in the pore, rather than being constant, becomes enhanced by the dielectric boundary and distorted by fixed charges. The presence of an ion further warps the field lines in the channel, and the field becomes continually deformed as the ion moves in. In the absence of any fixed charges on the protein or any mobile charge in the channel, the strength of the electric field across the channel induced by a membrane potential of 100 mV resembles a Gaussian curve (Fig. 4 *A*). It increases sharply from 2×10^6 V/m at the mouth of the channel to 32×10^6 V/m at the narrowest segment. To obtain this potential drop, a uniform field of strength 6×10^6 V/m has to be applied along the symmetry axis of the torus. Thus, compared to the applied field, the total electric field is nearly canceled in the mouth region, but is enhanced by more than fivefold near the neck region. This enhancement can be intuitively understood from the geometry: the field lines that represent the field strength are crowded into a smaller and smaller area as one approaches the narrow region of the channel. The potential change, in the absence of fixed and mobile charges, occurs mainly in the central 15–20 Å (Fig. 4 *B*).

The electric field and isopotential contours are further distorted when an ion is placed in the vestibule and dipoles are embedded in the protein. In Fig. 5, isopotential lines in the channel in the presence of dipoles are plotted. Four dipoles with a total moment of 100×10^{-30} Coulomb-meter are placed 5 Å above the midline (0 Å), and another four dipoles of the same strength are placed 5 Å below the midline. (Hereafter, Coulomb-meter will be abbreviated as Cm (1 Debye $= 3.33 \times 10^{-30}$ Cm).) The dipoles are located such that their negative charges are 2 Å inside the water-protein boundary, and their positive counterparts are 5 Å further inside the channel protein.

Fig. 5 *A* shows the potential in the absence of ions in the vestibule. The potential changes from 0 mV near the entrance of the vestibule to −180 mV at the midline, and then increases to −100 mV at the opposite end of the channel (Fig. 5 *A*). There is a pronounced asymmetry in the potential changes in the upper and lower halves of the channel. When a cation is moved along the central axis through the channel, the isopotential lines undergo profound changes. The changing patterns of electric potential as a cation moves from the upper vestibule to the midline and then to the lower vestibule are shown in Fig. 5, *B–D*. The electric potential in the entire upper vestibule becomes positive when a cation is

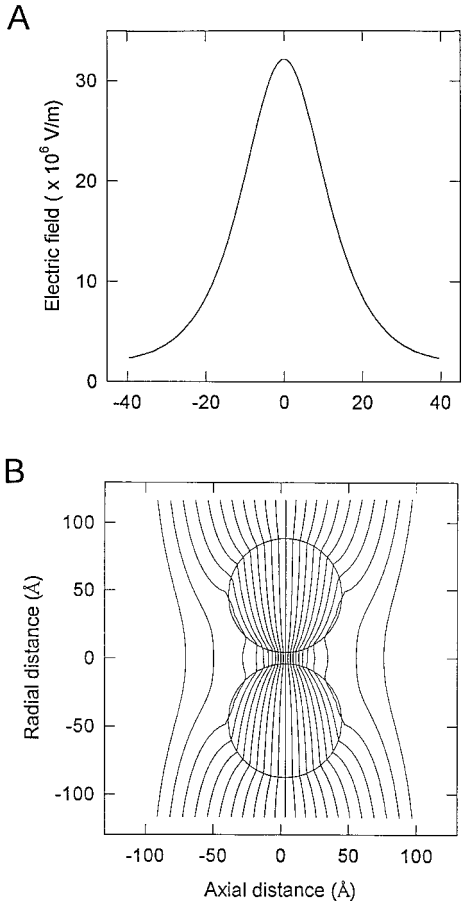

FIGURE 4 Electric field across the channel and isopotential profile. (*A*) The *z* component of the electric field resulting from an applied potential difference of 100 mV across the channel is plotted against the axial distance. (*B*) A potential difference of 100 mV maintained across the channel changes nonuniformly along the pore. The isopotential lines at the extreme left and right represent 0 and −100 mV, respectively. A potential drop of 4.5 mV is indicated by successive isopotential lines.

placed in the upper vestibule, at the central axis, 20 Å from the midline (Fig. 5 *B*). The potential rises from 0 mV outside the channel to +100 mV in the vicinity of the ion, falling to −160 mV near the upper ring of the dipoles, and then rising again to −100 mV at the other end of the channel. It is clear from this profile that a second cation in the vicinity of the vestibule already occupied by an ion will experience a repulsive potential, the magnitude of which will be further increased as its induced surface charges enhance this potential. Fig. 5 *C* shows the potential profile of the channel when a cation is moved to the midline (labeled 0 Å). The potential in the entire upper vestibule is slightly positive, slowly changing from 0 mV at its mouth to +20 mV near the constricted segment. In the narrow transmembrane region, the negative poles of the fixed charges on the protein wall interact with a positive charge in the center, which in turn induces surface negative charges. The potential in this region changes rapidly, rising steeply from +20 mV to +100 mV. The potential then declines from 0 mV to −100 mV in the lower vestibule. Finally, when a cation is moved into the lower vestibule, 20 Å below the midline, its influence on the potential profile in the upper reservoir becomes negligible (cf. Fig. 5, *A* and *D*). There is a local distortion of the potential lines in the vicinity of the ion.

These calculations clearly indicate that the potential profile and electric field in the channel depend in a sensitive way on the shape of the dielectric boundary and the location of the fixed charges in the protein. The profiles fluctuate dramatically with spatial variations of ions inside or in the vicinity of the channel. The uniform field assumption (under an applied field) is clearly not applicable to a vestibular shape.

Potential profiles presented to anions and cations

In Fig. 6 we show the potential energy barriers that ions have to surmount under various conditions. The trajectories of a cation moving from outside to inside (*left to right*) and an anion moving from inside to outside (*right to left*) are indicated as continuous and broken arrows, respectively, in the inset of Fig. 6 *A*. In the absence of any applied electrical field or fixed charges, the energy barriers presented by the image charges on the vestibular wall to a cation outside and an anion inside of the cell are identical, as indicated by the dotted line in Fig. 6 *A*. When a potential difference of 60 mV is applied between the inside and outside of the channel, driving the ions in the direction of the arrows, the heights of the energy barriers appearing to both cation and anion are lowered by $\sim 1\ kT_r$. The barriers appearing to a cation and anion are shown, respectively, as filled squares and open circles in Fig. 6 *A*. Thus in the presence of the membrane potential of −60 mV, a monovalent cation or anion whose kinetic energy is greater than $2.6\ kT_r$ will be able to move across the channel.

The channel becomes exclusively permeable to cations once charge residues are placed on the protein wall. The effects of dipoles placed on the protein wall of the constricted region are shown in Fig. 6 *B*. Four dipoles, positioned 90° apart and perpendicular to the *z* axis (or the long axis of the pore), are placed slightly to the left of the center, and an identical set of four dipoles is placed to the right (see the *inset* of Fig. 6 *B*). The total moment of four dipoles for the simulations shown in Fig. 6 *B* is 100×10^{-30} Cm or 30 Debyes. Viewed from a cation navigating from outside of the channel to inside (*left to right* in Fig. 6), the combined potential profile presented by the induced surface charges, the applied electrical field, and the dipoles on the channel wall is that of a well, and the net force exerted on it is an attractive force (*filled squares* in Fig. 6 *B*). In contrast, for an anion attempting to move in the opposite direction, there is an insurmountable energy barrier, the height of which is 33×10^{-21} J or $8.3\ kT_r$. The probability of an ion having a kinetic energy large enough to surmount such a barrier, given by the Boltzmann factor, is $\sim 10^{-4}$. From these simulations, we conclude that the cation-anion selectivity of a

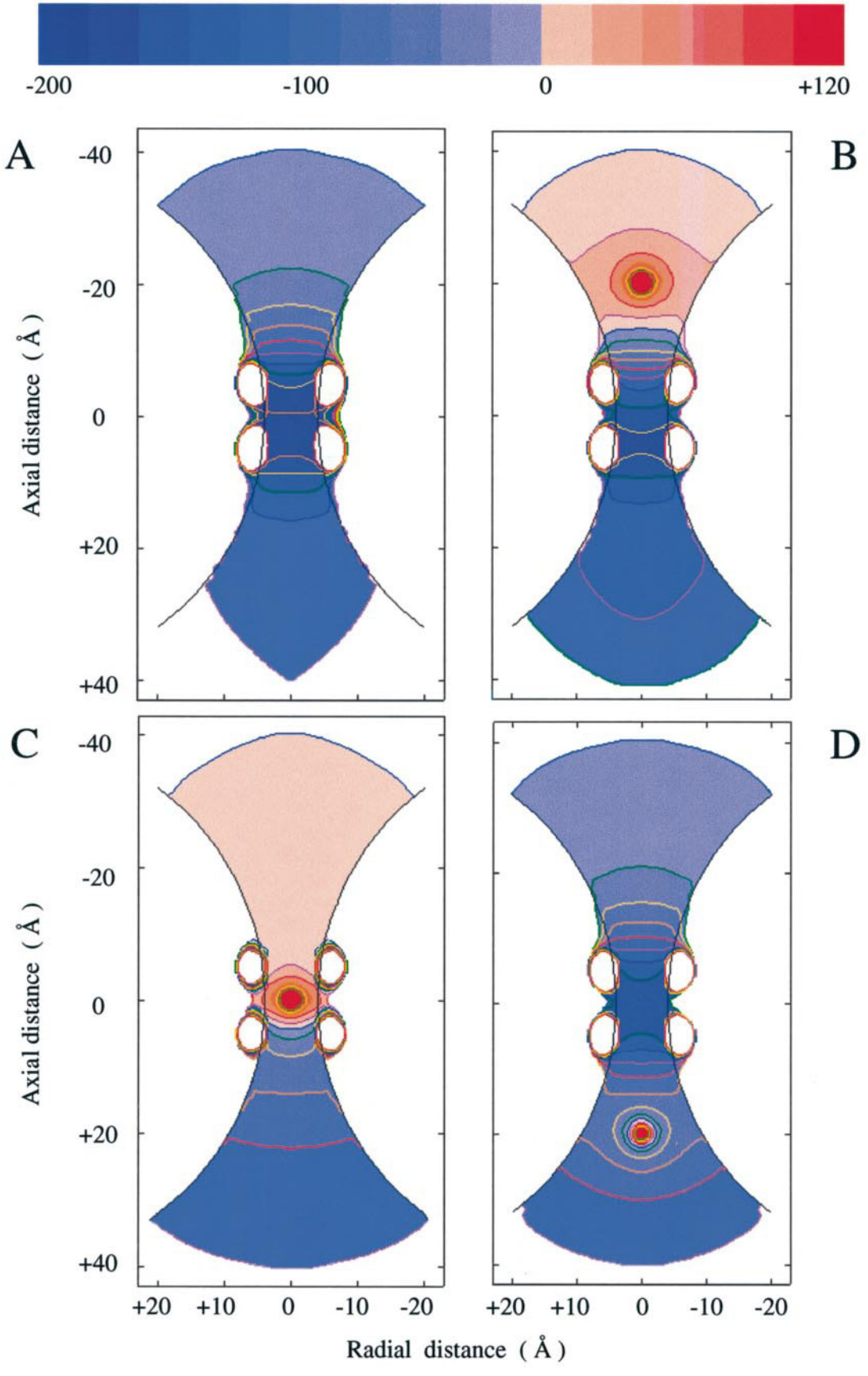

FIGURE 5 Isopotential contours in the presence of dipoles and a cation in the channel. Four dipoles with total moments of 100×10^{-30} Cm are placed on each side of the midline (at $z = \pm 5$ Å), and a transmembrane potential of 100 mV is applied across the channel. The resulting isopotential contour is

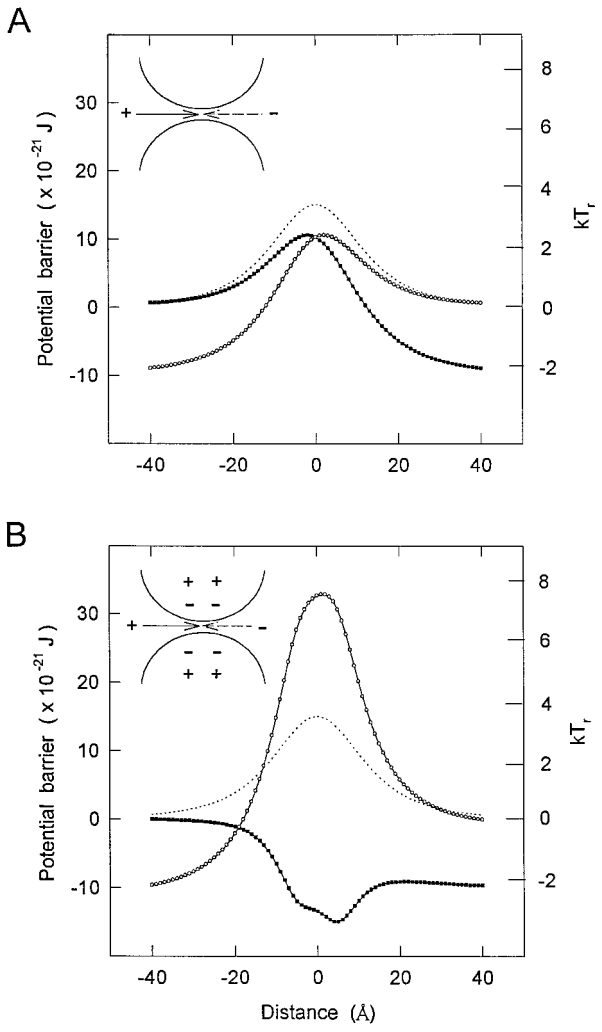

FIGURE 6 Elimination and enhancement of energy barriers by dipoles. In the absence of both dipoles and a potential difference, the barrier presented to a cation traversing left to right is the same as that presented to a cation traversing right to left, as indicated by dotted line in *A*. This line is also reproduced in *B* for ease of comparison. (*A*) When a potential difference of 60 mV is applied, the peak heights of barriers seen by a cation (●) and by an anion (○) are lowered. The barriers experienced by the two ionic species moving under the influence of the field are the same. (*B*) The placement of dipoles of 100×10^{-30} Cm at each side of the midline alters the shape of the barriers presented to a cation (●) and an anion (○). Dipoles are oriented such that their negative poles face the channel lumen.

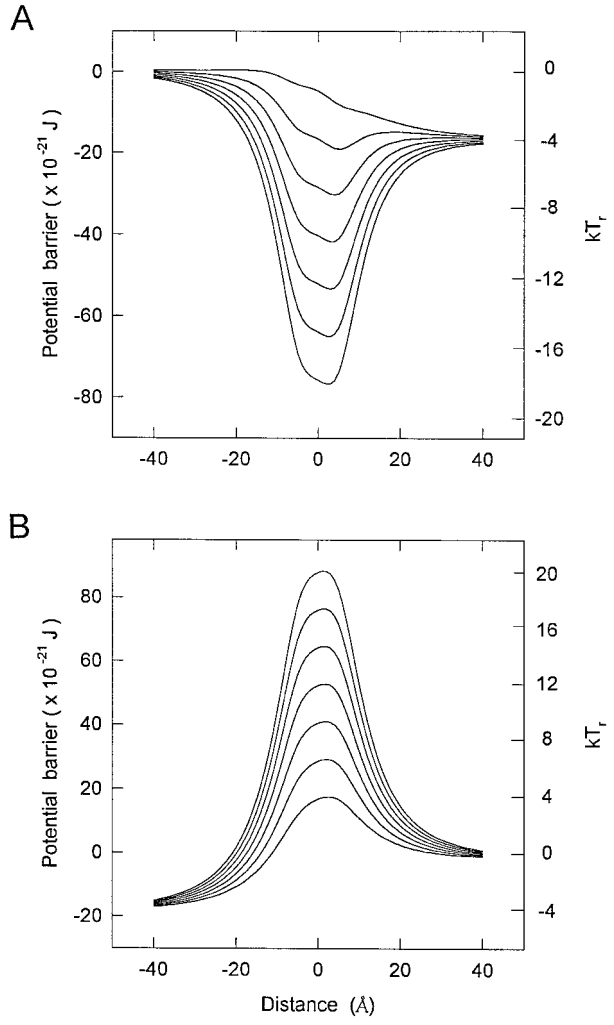

FIGURE 7 Changes in potential profiles with dipole strengths. A potential difference of 100 mV is applied across the channel, and then the potential energy of an ion as it moves along the central axis from $z = -40$ Å to $z = +40$ Å is determined. (*A*) The potential well seen by a cation becomes progressively deeper as the strength of the dipoles is changed from 50 to 350×10^{-30} Cm in steps of 50×10^{-30} Cm. (B). The potential barrier seen by an anion increases progressively as the strength of the dipoles increases from 50 to 350×10^{-30} Cm.

channel can, in theory, be achieved by the presence of a few charge residues near the constricted segment of the channel wall.

It is of interest to investigate how many charge residues near the constricted channel segment are needed to ensure that the channel would be impermeable to anions. Fig. 7 illustrates the systematic changes in the potential profile presented to an anion and a cation with the strength of dipole moments placed around the narrow channel segment.

shown in *A*, where the magnitude of the potential is represented by shades of blue. The potential across the channel changes from −20 mV (*pale blue*) in the upper vestibule to −180 mV (*deep blue*) near the constricted segment of the channel. It rises again to −80 mV (*light blue*) in the lower vestibule. In *B*, *C*, and *D*, a cation is placed on the central axis at $z = -20$ Å, $z = 0$ Å, and $z = +20$ Å, respectively. In *B*, the potential in the upper vestibule in the presence of a cation is predominantly positive, rising to +20 mV (*pale red*) near its wide region to +100 mV (*deep red*) in the vicinity of the ion. In *C*, with the ion on the midline, the potential in the upper vestibule in the main is positive, ranging from 0 mV near the entrance of the upper vestibule to +20 mV near the narrow segment of the channel. The ion at this position has little effect on the potential in the lower vestibule (cf. *A* and *C*). In *D*, the potential in the lower vestibule is slightly distorted by the presence of the ion. The potential countour in the upper reservoir is similar to that found in the absence of any ion in the channel (cf. *A* and *D*).

The applied potential difference across the channel is kept constant at 100 mV. The total moments of dipoles used to generate the curves shown in Fig. 7 *A* are increased systematically from 50 to 350 $\times$ 10^{-30} Cm. The peak heights of the potential barrier presented to an anion change from 16 to 90 $\times$ 10^{-21} J. Because the negative poles of the dipoles are pointing toward the channel lumen, a cation moving through it encounters a potential well, the depth of which increases with increasing dipole strengths (Fig. 7 *B*). When the dipoles, with a total strength of 350 $\times$ 10^{-30} Cm, are placed on the channel wall, the depth of the potential well created for a cation is -77×10^{-21} J.

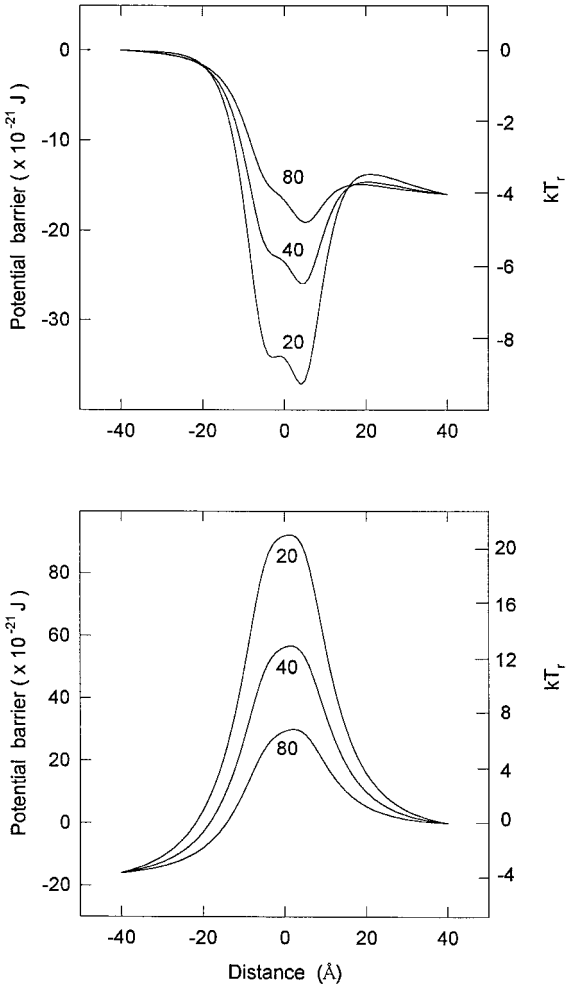

FIGURE 8 Changes in potential profiles with different dielectric constants. The potential profiles are calculated by using the same procedures as in Fig. 7, with a fixed dipole strength of 100 $\times$ 10^{-30} Cm and an applied potential difference of 100 mV. (*A*) The potential well seen by a cation traversing the channel is computed under the assumption that the dielectric constant of the fluid in the channel is first 80, then 40, and then 20. The well deepens as the dielectric constant is decreased. (*B*) The potential barrier seen by an anion increases progressively when the dielectric constant in the channel is changed from 80 to 40 and then to 20.

Change of the dielectric constant in the vestibule

In calculating the height of barriers, we assumed the dielectric constant of the vestibule to be 80, the same as that of bulk water. In reality, it is possible that the true value may turn out to be considerably lower than 80. If so, the magnitude of a true potential barrier will be higher than the one we provide here.

As an illustration, we compare in Fig. 8 the potential profiles obtained using three different values of dielectric constant. The applied electric potential is 100 mV, whereas the strength of dipoles is 100 $\times$ 10^{-30} Cm. The potential profiles seen by a cation moving from outside to inside (*left to right*) are shown in Fig. 8 *A*; the three curves are obtained by using the values of the dielectric constant of 80, 40, and 20. The depth of potential well increases as the dielectric constant decreases. Conversely, the height of potential barriers seen by an anion moving from inside to outside (right to left) increases as the dielectric constant decreases (Fig. 8 *B*).

The profiles shown in Fig. 8 are obtained under the assumption that the dielectric constant is reduced to 20 or 40 everywhere, including the reservoirs. If the dielectric constant of the reservoir is kept at 80 and that of the vestibule is reduced to a lower value, there will be an energy barrier for an ion entering the vestibule from the reservoir, resulting from the change in Born energy. The heights of the barriers presented to an ion with an effective radius of 3 Å moving from the reservoir to the vestibule with a dielectric constant of 40 or 20 will be, respectively, 1.2 kT_r and 3.5 kT_r.

DISCUSSION

The solution of Poisson's equation for a cylindrical geometry has been applied in the past to determine the height of the energy barrier and the transport mechanisms of ions across the gramicidin pore, porin, and gap junctions (Chen et al., 1997; Jordan, 1981; Levitt, 1978a,b). A representation of an ion channel as a cylindrical hole, which may be adequate for its short, constricted, transmembrane segment, does not capture the prominent feature of the nicotinic ACh receptor channel (Toyoshima and Unwin, 1988). The cross section of this channel deduced from the electron microscope picture shows a vestibule extending ~60 Å from the membrane into the extracellular space. Approximating the shape of such a vestibule as a surface generated by rotating a catenary around its symmetry axis, Hoyles et al. (1996) devised an iterative, numerical method of calculating the electric potential arising from a fixed charge near the dielectric boundary. They showed that an ion permeating such a model channel experiences a large repulsive force, owing to induced charges on the vestibular wall, and that the height of this energy barrier increases steeply as it moves toward the narrow neck region. This repulsive force can be counteracted by placing charge residues near the neck region of the channel. Thus it is clear that, to understand many of the salient properties of channels, a representation of a biological channel in any physical calculation must include, in

addition to the cylindrical transmembrane segment, the large extracellular domains that extend up to 60 Å above and below the membrane surface.

Obtaining numerical solutions of Poisson's equation satisfying the closed Dirichlet conditions for an arbitrary dielectric boundary requires a fairly large computational effort. With an ion located at a fixed position, the number of floating point operations required to calculate the magnitude of electric force is $\sim 10^9$. Nevertheless, the speed of modern computers is such that the shape and magnitude of a potential barrier presented to one ion permeating the channel can be readily determined by numerical methods. However, such static calculations of barrier heights are not very informative. Many interesting questions about channels, such as the effect of residual charges on the ionic concentration in vestibules, can only be answered unequivocally through dynamical simulations. In a realistic simulation, one needs two reservoirs of electrolyte solutions, one above and the other below the channel, with ~100 ions in each reservoir, and then one must run the simulation for around a million steps. Because ions execute a Brownian motion, rapidly changing their positions, the numerical computation of the field strengths has to be repeated at each step for every ion. Such a simulation, requiring more than 10^{17} floating point operations, is even beyond the powers of supercomputers. Thus implementation of the numerical solution in a dynamical simulation is not suitable for this task.

The analytical solution for Poisson's equation for a realistic channel geometry we present here is a prerequisite for dynamical studies of the ion transport problem. Although the toroidal channel differs somewhat from the shape of the acetylcholine channel deduced previously (Toyoshima and Unwin, 1988), the salient electrostatic properties of the biological channel are captured by this idealization. In this context, we note that the potential profile obtained from a toroidal channel does not differ appreciably from that obtained from a biconical or catenary channel (see Fig. 3). Thus the general conclusions derived by using the toroidal channel may remain valid for a more realistic geometry, such as catenary, although quantitative numerical estimates may differ slightly.

One such conclusion is the drastic effect the channel boundary has on an applied uniform electric field. The usual assumption in treating channel problems, which simplifies the solution enormously, is that the applied field remains uniform in the channel environment. Although this may be a reasonable approximation in some simple geometries such as a cylindrical pore, it is definitely not valid in a vestibular geometry where the total field exhibits a highly nonuniform behavior, as depicted here (Fig. 4). Another argument often made to justify the use of uniform electric field is that when one averages over long times, fluctuations in the electric field wash out, and one ends up with, more or less, a uniform field. Obviously, the time scale in such an averaging is very important, and its premises should be examined by dynamic simulation methods. Our initial Brownian dynamics calculations indicate that nonuniform fields induced by the boundary play a crucial role in determining ion motion in the vestibule, which raises doubts about the validity of time-average arguments (Li et al., 1997).

That charged amino acid residues play an important role in the anion-cation selectivity has been alluded to by, among others, Unwin (1989), who showed that a channel permeable to cations has more negatively charged amino residues in its primary sequence and, conversely, a channel permeable to anions has more positively charged amino residues. Our calculations show that a ring of negatively charged residues near the channel neck counteracts the repulsive dielectric force presented to a cation entering the vestibule, while raising the potential barrier for anions (Fig. 7). The height of the potential barrier for an anion increases steadily with the magnitude of the surface charges. At the same time, for a cation, the presence of excessive numbers of such fixed charges turns the potential barrier into a potential well, the depth of which increases with increasing magnitude of negative charges on the protein wall. If the depth of such a well is large, an ion moving into the vestibule may become trapped in it, as the applied electric field cannot provide a sufficiently large driving force to enable the ion to traverse the channel. It is possible that, in real biological channels, the number of charged amino acid residues on the constricted pore segment is sufficiently large to cancel the repulsive dielectric force, but not too large to detain an ion by its attractive force. This also ensures that the channel is virtually impermeable to counterions.

One of the uncertainties inherent in electrostatic calculations on model ion channels is the value of the dielectric constant in the channel. Chen et al. (1997), for example, used the customary value of 80 in modeling the synthetic channel composed of a bundle of six α-helices, which has a pore diameter of 8 Å and a length of 30 Å. In contrast, Bek and Jakobsson (1994) calculated the Coulomb repulsion between ions in a cylindrical channel, using a dielectric constant of 20. A biological vestibule contains ~500 water molecules, and when such a small number of molecules are confined in a space, some of the macroscopic properties of such "vicinal water" are known to differ appreciably from those determined in bulk water (Schufle et al., 1976; Drost-Hansen and Singleton, 1992). A small decrease in the dielectric constant of a liquid leads to a similar increase in the potential profile (see Fig. 8), but because the flux depends exponentially on the potential barrier, even a small increase could lead to a drastic reduction in the flux. Therefore, it is highly desirable to determine, perhaps by using molecular dynamics calculations, how the polarizability of water molecules changes as the volume containing them decreases. Such information is not currently available.

It must be emphasized that the electrostatic equations we use merely describe the phenomena at the macroscopic level and fail to have meaning microscopically. Implicit in Laplace's and Poisson's equations are the assumptions that ions can be idealized as point charges and the dielectric can be represented as a continuous medium. In a narrow cylindrical tube of ~4 Å radius, where the continuum assump-

tions are unlikely to be valid and an ion occupies an appreciable space, potentials computed with the electrostatic equations may prove to be poor approximations of the physical reality. For this reason, our estimates of the potential barrier at the narrow neck region, stretching ~10 Å at the midline, need to be revised by molecular dynamics simulations.

APPENDIX

Here we sketch the solution of the second-order difference equation (Eq. 20). For convenience, we will suppress the superscript m, but the same equation, with different coefficients q_n^m and λ_n^m, has to be solved for each value of m. The Green function corresponding to Eq. 20 satisfies (see Love, 1972)

$$G_{n+1,N} - q_n G_{n,N} + G_{n-1,N} = \delta_{n,N+1} - 2\cosh\mu_1\delta_{n,N} + \delta_{n,N-1} \tag{23}$$

for each value of N. Here $\delta_{n,N}$ denotes Kronecker delta. Solutions of Eq. 20 are then given by

$$E_n = \sum_{N=-\infty}^{\infty} G_{n,N}\lambda_N \tag{24}$$

as can be verified by substituting Eq. 24 in Eq. 20 and using Eq. 23.

Construction of the Green function in Eq. 23 is conceptually similar to the familiar cases in electrostatics. One first finds the solutions of the homogeneous equation,

$$G_{n+1,N} - q_n G_{n,N} + G_{n-1,N} = 0 \tag{25}$$

and then implements the "boundary conditions" implied in Eq. 23. The two independent solutions of Eq. 25 can be found from a study of its asymptotic form as $|n| \to \infty$. In that limit, $q \to 2\cosh\mu_1$, and the ratios $G_{n+1,N}/G_{n,N}$ for the solutions tend to $\exp(\pm\mu_1)$. The solutions of Eq. (25) with the correct asymptotics are given in terms of the continued fractions as (see, for details, Milne-Thompson, 1960)

$$\begin{aligned}\frac{G_{n+1,N}}{G_{n,N}} &= \cfrac{1}{q_{n+1} - \cfrac{1}{q_{n+2} - \cfrac{1}{q_{n+3} - \cdots}}} \equiv \alpha_{n+1}\\ \frac{G_{n-1,N}}{G_{n,N}} &= \cfrac{1}{q_{n-1} - \cfrac{1}{q_{n-2} - \cfrac{1}{q_{n-3} - \cdots}}} \equiv \beta_{n-1}\end{aligned} \tag{26}$$

Equation 26 can be written as recursion relations among α_n and β_n:

$$\alpha_n = \frac{1}{q_n - \alpha_{n+1}}, \quad \beta_n = \frac{1}{q_n - \beta_{n-1}} \tag{27}$$

which provide a simple method for their calculation by iteration. From the symmetry properties of $P^m_{n-1/2}$, $Q^m_{n-1/2}$ and their derivatives (they remain invariant under $n \to -n$), it follows that $q_{-n} = q_n$ in Eq. 19. Using this fact in Eq. 27, it is seen that $\alpha_n = \beta_{-n}$, and therefore only one set of coefficients needs to be calculated. Rewriting Eq. 26 as

$$\begin{aligned}G_{n+1,N} &= \alpha_{n+1}G_{n,N}, \quad n \geq N+1\\ G_{n-1,N} &= \beta_{n-1}G_{n,N}, \quad n \leq N-1\end{aligned} \tag{28}$$

$G_{n,N}$ can be determined from Eq. 28 recursively, once $G_{N+1,N}$ and $G_{N-1,N}$ are specified. To calculate these two quantities, we use the "boundary conditions" on Eq. 23 at $n = N-1, N, N+1$, which gives the following equations:

$$\begin{aligned}(\beta_{N-2} - q_{N-1})G_{N-1,N} + G_{N,N} &= 1\\ G_{N-1,N} - q_N G_{N,N} + G_{N+1,N} &= -2\cosh\mu_1\\ G_{N,N} + (\alpha_{N+2} - q_{N+1})G_{N+1,N} &= 1\end{aligned} \tag{29}$$

where we have substituted $G_{N-2,N} = \beta_{N-2}G_{N-1,N}$ and $G_{N+2,N} = \alpha_{N+2}G_{N+1,N}$ from Eq. 28. These equations can be further simplified by using $\beta_{N-2} - q_{N-1} = -1/\beta_{N-1}$ and $\alpha_{N+2} - q_{N+1} = -1/\alpha_{N+1}$, which follow from Eq. 27. Solution of the set of linear equations in Eq. 29 yields

$$\begin{aligned}G_{N-1,N} &= \frac{(2\cosh\mu_1 - q_N)\beta_{N-1}}{q_N - \alpha_{N+1} - \beta_{N-1}}\\ G_{N,N} &= \frac{(2\cosh\mu_1 - \alpha_{N+1} - \beta_{N-1})}{q_N - \alpha_{N+1} - \beta_{N-1}}\\ G_{N+1,N} &= \frac{(2\cosh\mu_1 - q_N)\alpha_{N+1}}{q_N - \alpha_{N+1} - \beta_{N-1}}\end{aligned} \tag{30}$$

Substituting Eqs. 28 and 30 in Eq. 24, we finally obtain for the coefficients E_n,

$$\begin{aligned}E_n = \sum_{N=-\infty}^{\infty} &\frac{\lambda_N}{(q_N - \alpha_{N+1} - \beta_{N-1})}\\ &\cdot\Bigg\{(2\cosh\mu_1 - \alpha_{N+1} - \beta_{N-1})\delta_{n,N} + (2\cosh\mu_1 - q_N)\\ &\cdot\left[\theta(n-N)\prod_{k=N+1}^{n}\alpha_k + \theta(N-n)\prod_{k=n}^{N-1}\beta_k\right]\Bigg\}\end{aligned} \tag{31}$$

where $\theta(x)$ is the step function, i.e., $\theta(x) = 1$ if $x > 0$, and 0 otherwise.

This work was supported by grants from the Australian Research Council and the National Health and Medical Research Council of Australia. The calculations upon which this work is based were carried on the Fujitsu VPP-300 of the ANU Supercomputer Facility. A vectorized computer program that gives the analytical solution of Poisson's equation for a toroidal geometry is available from the authors upon request.

REFERENCES

Bek, S., and E. Jakobsson. 1994. Brownian dynamics study of a multiply-occupied cation channel: application to understanding permeation in potassium channel. *Biophys. J.* 66:1028–1038.

Chen, D., J. Lear, and R. Eisenberg. 1997. Permeation through an open channel: Poisson-Nernst-Planck theory of a synthetic ion channel. *Biophys. J.* 72:97–116.

Drost-Hansen, W., and J. L. Singleton. 1992. Our aqueous heritage: evidence for vicinal water in cells. *In* Fundamentals of Medical Cell Biology, Vol. 3A. E. E. Bittar, editor. JAI Press, Greenwich, CT. 157–180.

Hoyles, M., S. Kuyucak, and S. H. Chung. 1996. Energy barrier presented to ions by the vestibule of the biological membrane channel. *Biophys. J.* 70:1628–1642.

Jordan, P. C. 1981. Energy barriers for passage of ions through channels. Exact solution of two electrostatic problems. *Biophys. Chem.* 13: 203–212.

Jordan, P. C. 1982. Electrostatic modeling of ion pores. Energy barriers and electric field profiles. *Biophys. J.* 39:157–164.

Jordan, P. C. 1983. Electrostatic modeling of ion pores. II. Effects attributable to the membrane dipole potential. *Biophys. J.* 41:189–195.

Levitt, D. G. 1978a. Electrostatic calculations for an ion channel. I. Energy and potential profiles and interactions between ions. *Biophys. J.* 22: 209–219.

Levitt, D. G. 1978b. Electrostatic calculations for an ion channel. II. Kinetic behavior of the gramicidin A channel. *Biophys. J.* 22:221–248.

Li, S. C., M. Hoyles, S. Kuyucak, and S.-H. Chung. 1997. Brownian dynamics study of ion transport in the vestibule of membrane channels. *Biophys. J.* 74:37–47.

Love, J. D. 1972. The dielectric ring in a uniform, axial, electrostatic field. *J. Math. Phys.* 13:1297–1304.

Milne-Thompson, L. M. 1960. The Calculus of Finite Differences. Macmillan and Co., London.

Morse, P. M., and H. Feshbach. 1953. Methods of Theoretical Physics, Vol. 2. McGraw-Hill, New York.

Roux, B., and M. Karplus. 1991. Ion transport in a model gramicidin channel: structure and thermodynamics. *Biophys. J.* 59:961–981.

Schufle, J. A., C.-T. Huang, and W. Drost-Hansen. 1976. Temperature dependence of surface conductance and a model of vicinal (interfacial) water. *J. Colloid Interface Sci.* 54:184–202.

Toyoshima, C., and N. Unwin. 1988. Ion channel of acetylcholine receptor reconstructed from images of postsynaptic membranes. *Nature.* 336: 247–250.

Unwin, N. 1989. The structure of ion channels in membranes of excitable cells. *Neuron.* 3:665–676.